Supporting Information

Single-Ion Negative-Charge Accelerator Unlocks High-Speed Li-ion Transport in In-Situ Polymerized Solid-State Lithium Metal Batteries

Jiajie Pan [1], Lingcai Zeng [2], Hao Wu [2], Tengrui Wang [2], Jieying Hua [2], Junhao Li [3], Kaixiang Shi [2], Rui Zhang [4], Yonggang Min [1, *] and Quanbing Liu [2, *]

[1] School of Materials and Energy, Guangdong University of Technology, Guangzhou 510006, China.

[2] Guangzhou Key Laboratory of Clean Transportation Energy Chemistry, Guangdong Provincial Key Laboratory of Plant Resources Biorefinery, School of Chemical Engineering and Light Industry, Guangdong University of Technology, Guangzhou 510006, China.

[3] School of Environmental and Chemical Engineering, Foshan University, Foshan 528225, China

[4] Department of Chemical Engineering, Tsinghua University, Beijing 100084, China

* Corresponding author. E-mail address:
ygmin@gdut.edu.cn (Y. Min), and liuqb@gdut.edu.cn (Q. Liu).

I. Supplementary Text

1. Experimental section

1.1. Materials

LiTFSI, DOL, and LiCl were sourced from Shanghai Aladdin Biochemical Technology Co., Ltd. LiDFOB was purchased from Shanghai Macklin Biochemical Co., Ltd. DME and Montmorillonite (MMT) were obtained from Suzhou DuoDuo Chemical Reagent Co., Ltd. $LiFePO_4$ (LFP) and Li foil were purchased from Guangdong Canrd New Energy Technology Co., Ltd. $LiNi_{0.8}Co_{0.1}Mn_{0.1}O_2$ (NCM811) was obtained from Ningbo Ronbay New Energy Technology Co., Ltd. The purchased reagents and solvents are of analytical grade and can be used directly without further purification.

1.2 Preparation of LMMT.

The LMMT was prepared by the cation exchange method: Firstly, the MMT bulk material was exfoliated into nanosheets through continuous ball milling. The 2.00 g MMT nanosheets and LiCl (4.239 g) were then dispersed in 100 mL of ethanol. The resulting mixture was stirred at 50°C for 1 hour to complete the ion exchange reaction. Subsequently, solid-liquid separation is achieved through vacuum filtration, followed by multiple ethanol washes to remove residual ionic impurities. Finally, subsequently subjected to freeze-drying (−50°C, 12 h) and vacuum-drying (100°C, 12 h) to ensure complete dehydration and stabilization of the interlayer structure.

1.3. Preparation of LMPDOL and PDOL precursor solution.

Firstly, 0.431 g LiTFSI was completely dissolved in the mixed solution, which consisted of 1 mL DOL and 0.1 mL DME. And then, 0.03 g LMMT was added to the mixed solution and stirred continuously to achieve nanoscale dispersion. Next, 0.2 M LiDFOB was added to the homogenized system while stirring continuously. After complete dissolution, the LMPDOL precursor solution was obtained. The PDOL precursor solution was prepared by the same process without LMMT nanosheets. Notably, this precursor solution was injected into cells.

1.4. Materials characterizations

Transmission electron microscope (TEM, Tecnai G2 F30) was used to characterize the morphology of LMMT. Images of the surface morphologies of Li were performed by field emission scanning electron microscope (FESEM, ZEISS sigma 500). X-ray diffraction (XRD) patterns were collected using a Rigaku mini flex 600 with Cu-K_α radiation (λ = 0.15418 nm) at 40 kV and 30 mA. The scans for 2θ values were recorded at 10° min^{-1} between 2° and 80°. Fourier transform infrared (FTIR) spectra were recorded using a Nicolet 6700 spectrometer in attenuated total reflection (ATR) mode. Raman spectra were collected by laser ultraviolet Raman spectrometer (LabRAM HR800). X-ray photoelectron spectroscopy (XPS, Thermo Fisher Escalab 250Xi) measurements were conducted to analyze the surface chemistry and elemental valence. Zeta potential was measured by using a Zetasizer Nano-ZS potential analyzer.

1.5. Electrochemical measurements

CR2032-type coin cells were assembled to investigate all the electrochemical performance in an Ar-filled glovebox (the content of O_2 and H_2O < 0.1 ppm). 25 μL of LMPDOL or PDOL precursor solution was immediately injected into the separator, and the cell was assembled and sealed. The precursor solution subsequently underwent spontaneous polymerization in the cell to form the LMPDOL and PDOL electrolytes. The cells were tested after resting for 48 h at room temperature. For Li|IPSE|Cu half cells were assembled with copper foils (13 mm of diameter) as the working electrodes and Li foils (12.5 mm of diameter, 500 μm thickness) as the counter/reference electrodes. For Li||Li symmetric cells were assembled with Li foils (12.5 mm of diameter, 500 μm thickness) as both anodes and cathodes. For full cells, the cathode slurry was obtained by mixing the active material with Poly (vinylidene fluoride) (PVDF) binder and conductive super-p in N-methyl-2-pyrrolidone (NMP) at a mass ratio = 8:1:1 and then pasted onto a piece of aluminum foil. After drying in vacuum at 100°C for 12 h and punching into diameter of 13 mm disks, the areal mass loadings of the obtained cathodes were approximately 3.2 mg cm^{-2} (LFP) and 7 mg cm^{-2} (NCM811). And the operating voltage range is 2.8 ~ 4.0 V (LFP) and 2.8 ~ 4.3 V (NCM811). For the pouch-type cells assembling, the cathode is commercial LFP

electrode (40 × 50 mm with a mass loading of 12.3 mg cm^{-2}), and the anode is an ultrathin Li film (45 × 55 mm rectangle with a thickness of 50 μm) on Cu foil. The pouch cells were assembled and sealed in a laminated aluminum film bag.

The cells were tested galvanostatically using a Neware battery testing system (CT-4008). The Tafel test was conducted on an AutoLab (PGSTAT302N) electrochemical workstation with the Li|IPSE|Li symmetric cells. The electrochemical impedance spectra (EIS) measurements were conducted on an AutoLab (PGSTAT302N) electrochemical workstation over a frequency range from 100 kHz to 0.1 Hz with an amplitude of 5 mV.

The time-dependent EIS during the in-situ polymerization process were testd based on Li|LMPDOL|LFP and Li|PDOL|LFP full cells (40 min per point). The variation in impedance (ΔR) was calculated by the following Equation:

$$\Delta R = R(t) - R(t-\Delta t)$$

$$R = R_b + R_{SEI} + R_{ct}$$

Where Δt is the measurement interval, R_b, $R_{SEI,}$ and R_{ct} are the resistance values of the bulk electrolyte, interface, and the charge transfer, respectively.

The electrochemical stability window of the LMPDOL and PDOL was tested by linear sweep voltammetry (LSV) on a coin cell with Li metal as anode and stainless steel (SS) as cathode. The potential range is 3.0 to 6.0 V with a scan rate of 10 mV s^{-1}.

The ionic conductivities of the electrolyte were measured by EIS using a SS blocking cell (SS|IPSE|SS). The intrinsic ionic conductivity (σ) of the SSE was calculated based on the EIS results using Equation:

$$\sigma = \frac{L}{R_b S}$$

Where R_b is the resistance value of the bulk electrolyte, L is the thickness of the IPSE, and S represents the effective contacting area between IPSE and SS.

The activation energy (E_a) was obtained by calculating resistance at a temperature range from 30 to 70°C according to the Arrhenius law:

$$\sigma = Aexp(-E_a/RT)$$

Where A is the pre-exponential factor, E_a is the activation energy for ion hopping, R is

the gas constant, and T is the absolute temperature.

Li-ion transference number (t_{Li^+}) of the electrolyte was measured in a symmetric Li|IPSE|Li cell with a direct-current (DC) polarization voltage of 10 mV associated with the AC impedance measurement, and then calculated by the following equation:

$$t_{Li^+} = \frac{I_S(\Delta V - I_0 R_0)}{I_0(\Delta V - I_S R_S)}$$

Where ΔV is the applied voltage (10 mV), I_0 and I_S are the initial and steady-state currents, respectively, R_0 and R_S are the initial and steady-state resistances of the Li|SSE|Li obtained by AC impedance, respectively.

1.6. Theory calculation

The first-principles calculations based on density functional theory (DFT) calculations were performed by using the GPU-accelerated Vienna Ab initio Simulation Package (VASP) in conjunction with the projector augmented wave (PAW) generalized gradient approximations (GGA) of Perdew-Burke-Ernzerhof (PBE). The relaxation convergence for electrons was 1×10^{-5} eV and the force convergence standard set to 0.03 eV $Å^{-1}$, which were achieved with the cut-off energy of 500 eV. The crystal structures and isosurfaces were visualized by using the VESTA package. The adsorption models were set up with a vacuum space of 15 Å to avoid the coupling between periodically neighboring structures. The Brillouin zone was sampled with Monkhorst mesh 3 × 3 × 1 throughout the computational process. To account for van der Waals (vdW) interactions, the DFT-D3 method was employed. The transition states and kinetic barriers of Li-ion diffusion were calculated by the CI-NEB method. The adsorption energy (E_{ads}) of adsorbates on the surface was calculated using the following equation:

$$E_{ads} = E_{total} - E_{sub} - E_{ads*}$$

Where E_{ads}, E_{sub}, and E_{ads*} are the total energy of the system with adsorbates on the surface, the pristine surface, and adsorbates, respectively.

1.7. Finite Element Method Simulation

The finite element method simulation was executed with COMSOL Multiphysics 5.6 software to simulate the lithium electrodeposition behavior and Li-ion

concentration. The simulation employed both the tertiary current distribution and deformed geometry modules. The corresponding governing equations used for the calculations are summarized below.

In the electrolyte, the mass transport of Li-ion and other species through diffusion, migration, and convection was described by comprehensively solving the Nernst-Planck equation:

$$N_{Li+} = -D_{Li+}\left(\nabla c_0 - \frac{zFc_0}{RT}\nabla\Phi\right)$$

where N_{Li}^+ is Li-ion flux, D_{Li}^+ is the diffusion coefficient of Li-ion, z is the charge of Li-ion, c_0 is the concentration of Li-ion, F represents the Faraday's constant, R is the ideal gas constant, T denotes the Kelvin temperature, and Φ corresponds to the electrolyte potential. In this work, the species concentrations satisfy the electroneutrality assumption. The steady-state spatial distribution of lithium ions along the diffusion layer was calculated, and the post-processed results are presented as contour plots.

The deposition rate of Li is determined by the local current density, as defined by the Butler-Volmer formulation:

$$i = i_0\left[exp\left(\frac{\alpha_a F\eta}{RT}\right) - \frac{c_{Li+}}{c_0}exp\left(\frac{\alpha_c F\eta}{RT}\right)\right]$$

where i_0 is exchange current density, η is overpotential, α_a and α_c are the anodic and cathodic charge transfer coefficients, respectively, and c_{Li}^+ is the concentration of Li-ion near the interface

A two-dimensional geometric model is established. The geometry is meshed with a free quadrilateral grid, with model dimensions of 6 μm × 6 μm. The rectangular (50 nm × 500 nm) arrays with specific Young's modulus and ionic conductivity were fabricated to simulate LMMT nanosheets. The electrochemical parameters were defined based on the overall properties of the electrolyte matrix rather than assigning values to individual filler components. The temperature was held constant during simulation.

II. Supplementary Fig.s

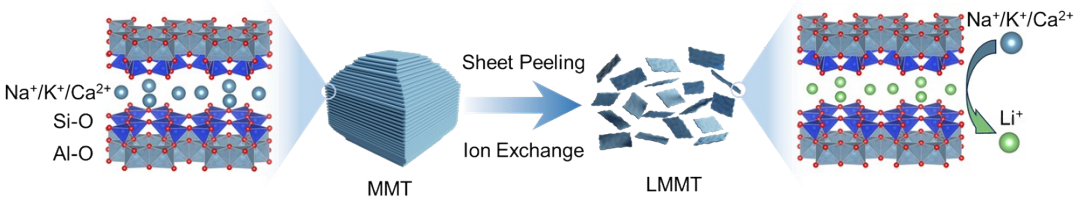

Fig. S1 Schematic representations of the MMT and LMMT structures.

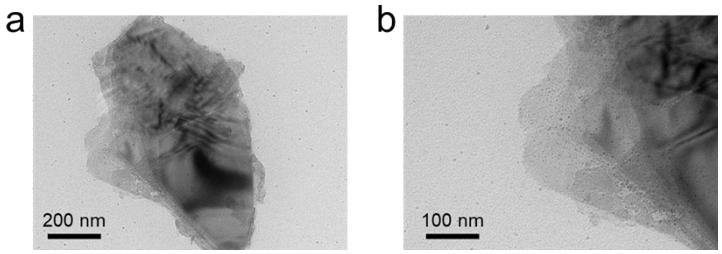

Fig. S2 TEM images of LMMT nanosheet.

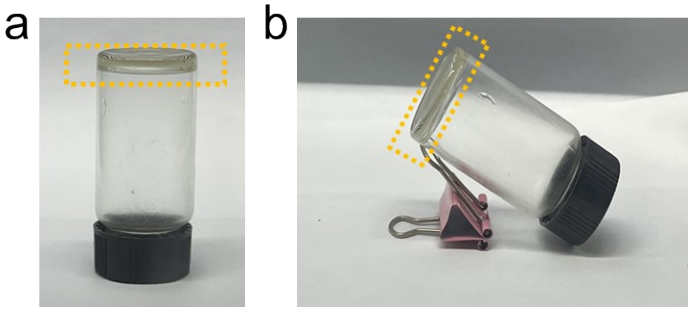

Fig. S3 Digital photographs of LMPDOL electrolyte after polymerization.

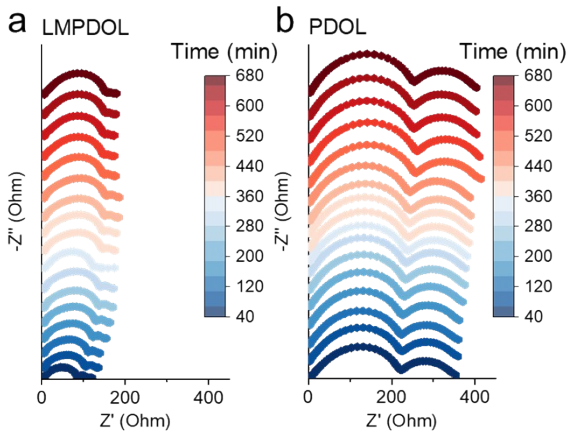

Fig. S4 Time-dependent EIS testing of (a) LMPDOL and (b) PDOL electrolytes during the in-situ polymerization process.

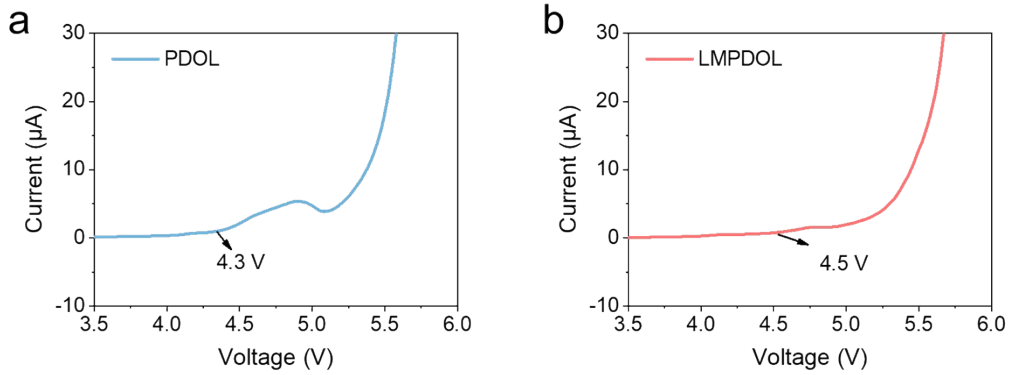

Fig. S5 LSV diagram of the (a) PDOL and (b) LMPDOL electrolytes.

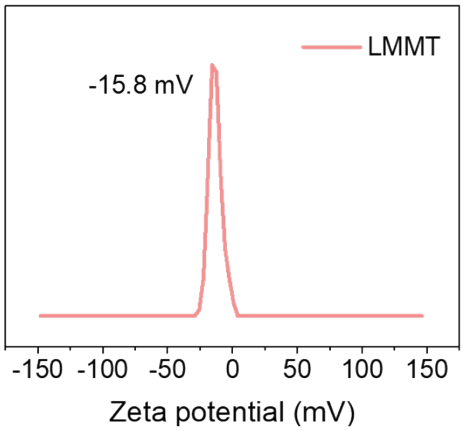

Fig. S6 Zeta potential of LMMT.

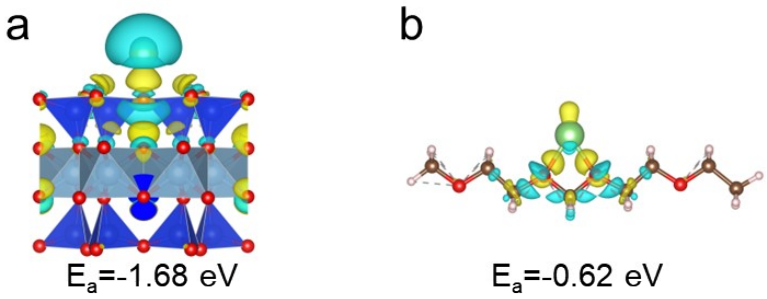

Fig. S7 Adsorption energies of Li-ion on (a) MMT and (b) PDOL.

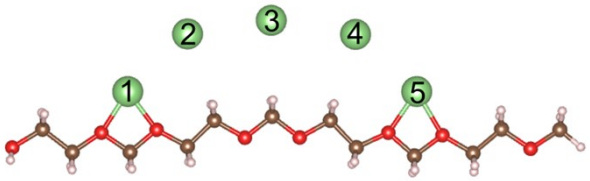

Fig. S8 Li-ion migration path on PDOL.

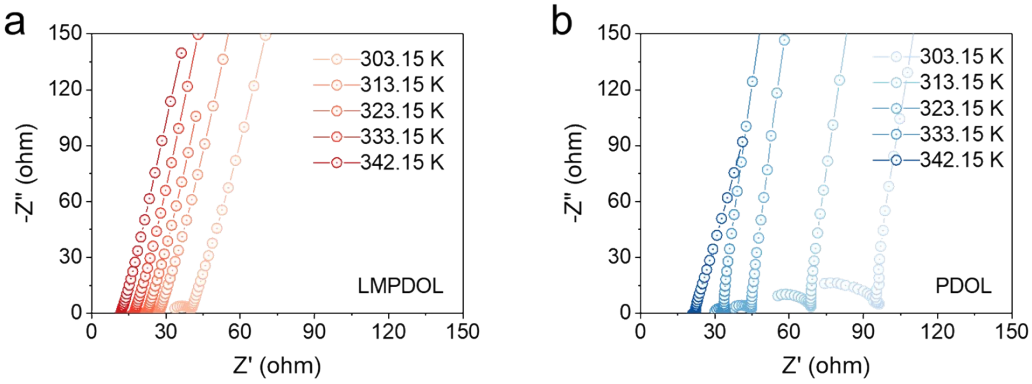

Fig. S9 Nyquist plots of (a) LMPDOL and (b) PDOL from 30 to 70°C.

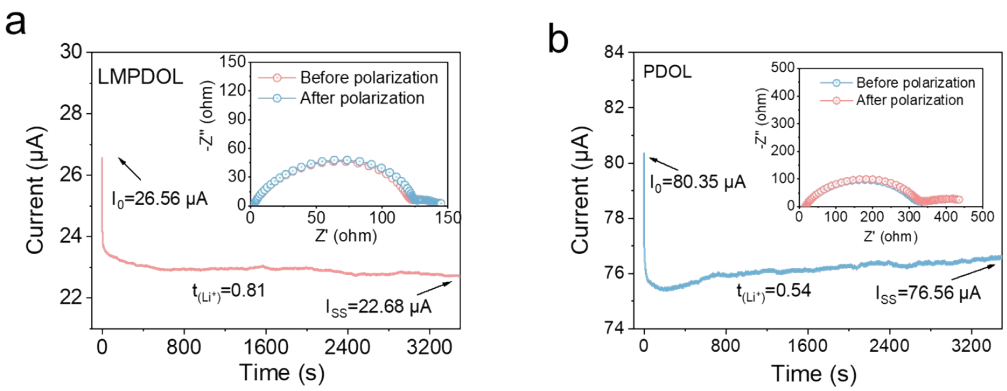

Fig. S10 Li-ion transference number (t_{Li}^{+}) of (a) LMPDOL and (b) PDOL.

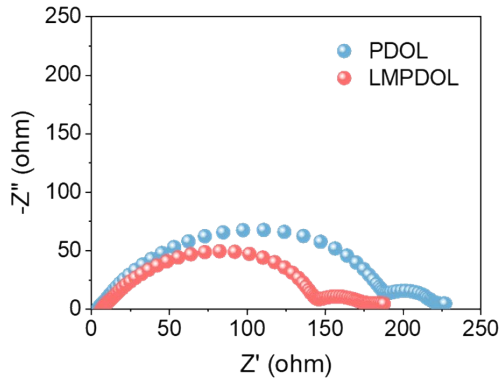

Fig. S11 Nyquist plots of symmetric cells based on PDOL and LMPDOL.

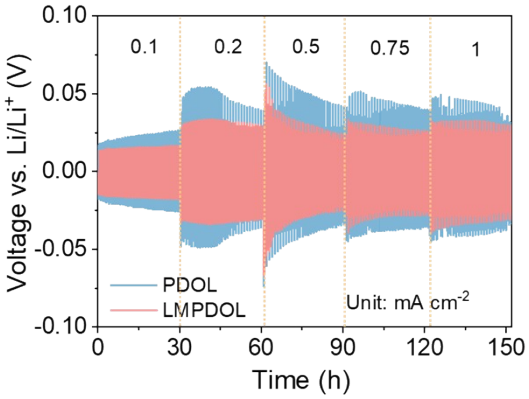

Fig. S12 Rate performance of the Li||Li symmetric cells with PDOL and LMPDOL electrolytes.

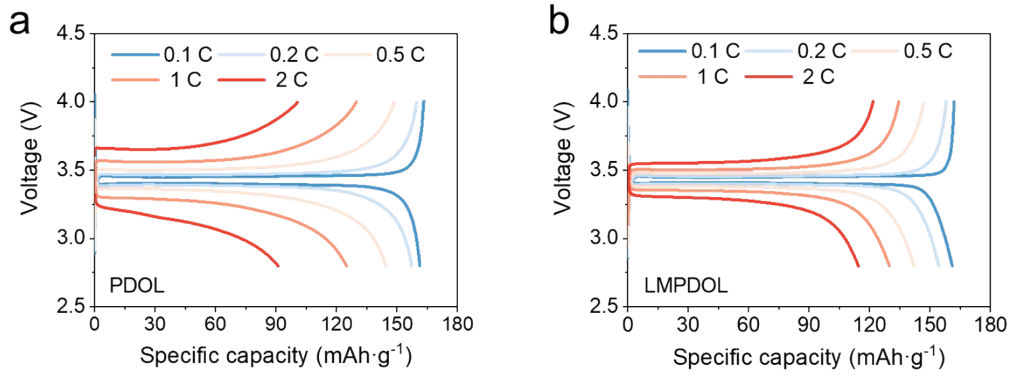

Fig. S13 Charge-discharge voltage curves at different current densities for (a) Li|PDOL|LFP and (b) Li|LMPDOL|LFP coin cells.

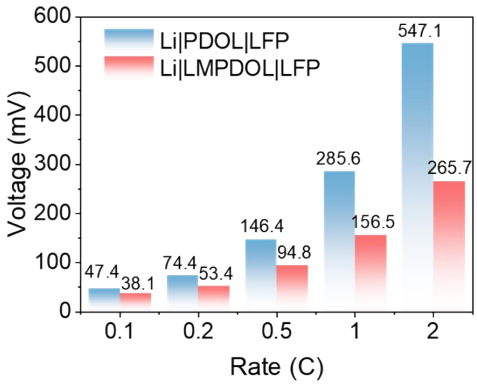

Fig. S14 The polarization voltages of Li|LMPDOL|LFP and Li|PDOL|LFP under different current densities.

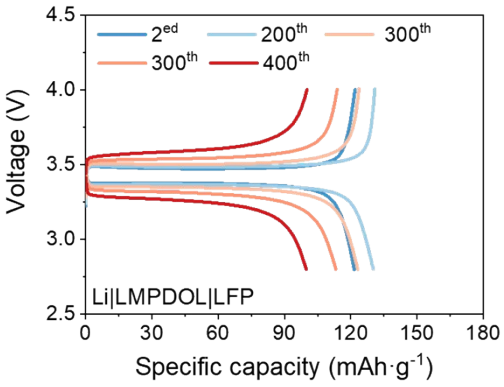

Fig. S15 Charge-discharge voltage curves of Li|LMPDOL|LFP pouch cell at 0.2 C.

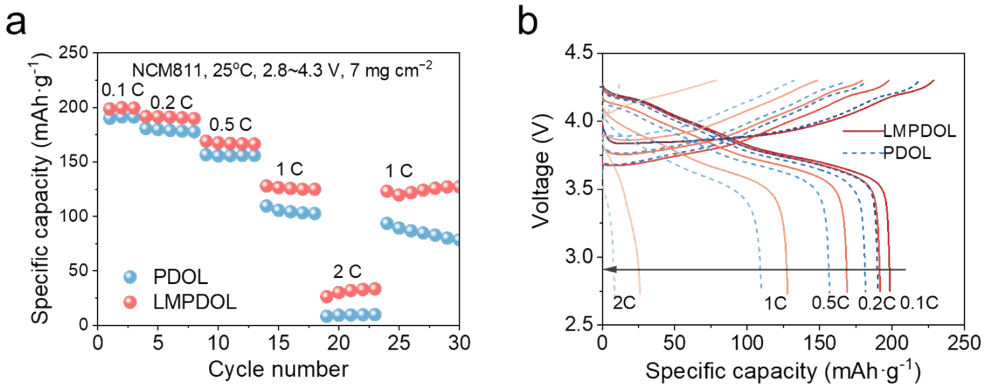

Fig. S16 Rate performance of Li|LMPDOL|NCM811 and Li|PDOL|NCM811.

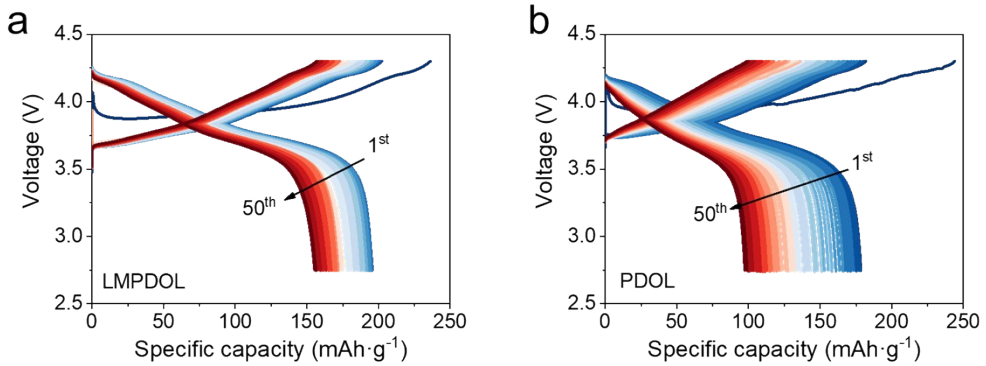

Fig. S17 Charge-discharge voltage curves of Li|LMPDOL|NCM811 cell at 0.2 C.

II. Supplementary Tables

Table S1. The equivalent circuit of time-dependent EIS and the corresponding value of R and ΔR for LMPDOL and PDOL during the in-situ polymerization process.

Equivalent circuit			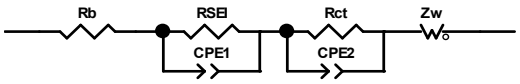		
LMPDOL			PDOL		
Time (min)	R (Ω)	ΔR (Ω)	Time (min)	R (Ω)	ΔR (Ω)
40	108	-	40	354.78	-
80	133.09	19.79	80	359.66	4.88
120	157.75	5.3	120	360.04	0.38
160	166.21	14.88	160	362.2	2.16
200	168.97	9.78	200	370.62	8.42
240	171.72	7.66	240	376.09	5.47
280	**173.44**	**0.8**	280	377.86	1.77
320	**173.17**	**0.78**	320	381.59	3.73
360	**173.23**	**1.98**	360	385.99	4.4
400	354.78	1.62	**400**	**388.49**	**2.5**
440	360.04	1.13	**440**	**389.9**	**1.41**
480	370.62	2.04	**480**	**388.4**	**-1.5**
520	377.86	-0.32	520	402.4	14
560	385.99	0.08	560	404.1	1.7
600	389.9	-0.35	600	404.11	0.01
640	402.4	0.25	640	402.38	-1.73
680	404.11	-0.19	680	403.77	1.39

Table S2. Cycling performance of symmetric cells with LMPDOL electrolyte in this work compared with other PDOL-based electrolytes reported in recent literature.

Electrolyte	Current density (mA cm^{-2})	Deposition capacity (mAh cm^{-2})	Cycling time (h)	Ref.
CPDOL-DMA	0.1	0.1	200	1
PBA-PDOL	0.1	0.05	900	2
DTSPE	0.1	0.1	1000	3
PFP@PDOL	0.2	0.2	1200	4
GPE-PVDF@LATP	0.2	0.2	600	5
PDOL@LLTO	0.2	0.2	1000	6
BN/PVDF@PDL	0.2	0.1	1000	7
PLLDR	0.2	0.2	1000	8
SiO_2+MMT+PDOL	0.2	0.2	1200	9
PTADOL	0.25	0.25	1300	10
TPDOL@FEC	0.1	0.1	1000	11
S-LLZTO/PDOL	0.1	0.1	1000	12
PDOL+YSZ	0.1	0.2	1100	13
TPDOL	0.2	0.2	1500	14
LMPDOL	**0.2**	**0.2**	**1700**	**This work**

References

1 K. Chen, X. Shi, Y. Shen, B. Gou, L. Yang, Y. Li, J. Gong, Y. Wang, J. Chai, Y. Zheng, W. Zhang and Z. Liu, *Small*, 2025, **21**, e2504201.

2 Q. Chen, Y. Liang, Q. Zhang, H. Liu, S. Wu and H. Duan, *Chem. Eng. J.*, 2025, **519**, 165235.

3 L. Liu, J. Xue, Y. Gao, S. Zhang, H. Zhang, K. Peng, X. Zhang, S. Lu, S. Weng, H. Tu, Y. Liu, Z. Wang, F. Zhang, D. Fu, J. Xu, Q. Luo and X. Wu, *Mater. Rep. Energy*, 2025, **5**, 100311.

4 S. Liu, Y. Yan, S. Zhang, D. Yan, Y. Cai, S. Yin, Q. Lu, W. Ren, Q. Zhang and Y. Xing, *Energy Storage Mater.*, 2025, **80**, 104396.

5 D. Yang, Y. Yang, Y. Sun and T. Zhang, *Adv. Funct. Mater.*, 2025, **35,** 2420202.

6 X. Yang, C. Sun, R. Li, N. Pei, X. Li, Y. Deng, P. Zhang, J. Lin and J. Zhao, *Chem. Eng. J.*, 2025, **520**, 165754.

7 T. Zhu, G. Wang, J. Hou, W. Sun, C. Song, Q. Yuan, C. Zhang, X. Lei, Y. Su, M. Chen, Y. Song and J. Zhao, *Adv. Funct. Mater.*, 2025, **35,** 2501870.

8 C. Lei, T. Zhou, M. Zhang, T. Liu, C. Xu, R. Wang, X. He and X. Liang, *Adv. Sci.*, 2024, **11**, e2405482.

9 G. Lin, T. Yang, H. Zhang, H. Wang, W. Zhang, H. Huang, Y. Xia, X. Xia, X. Tao and J. Zhang, *Chem. Eng. J.*, 2024, **488**, 151161.

10 Y. Du, L. Zhao, C. Xiong, Z. Sun, S. Liu, C. Li, S. Hao, W. Zhou and H. Li, *Energy Storage Mater.*, 2023, **56**, 310–318.

11 S. Liu, B. Wu, S. Huang, Z. Lin, H. Song, L. Du, Z. Liang and Z. Cui, *Adv. Energy Mater.*, 2025, **15**, 2402848, 2402848.

12 L. Cui, S. Zhang, J. Ju, S. Liu, H. Wang, J. Xu, W. Zhang, P. Mu, Y. Zhang, L. Liu, P. Xu, P. Han, Z. Lv and G. Cui, *Angew. Chem. Int. Ed.*, 2025, e202517153.

13 H. Yang, B. Zhang, M. Jing, X. Shen, L. Wang, H. Xu, X. Yan and X. He, *Adv. Energy Mater.*, 2022, **12**, 612, 2201762.

14 S.-J. Yang, H. Yuan, N. Yao, J.-K. Hu, X.-L. Wang, R. Wen, J. Liu and J.-Q. Huang, *Adv. Mater.*, 2024, **36**, e2405086.